OPEN ACCESS

University of BRISTOL

Diaz, A., Ehn, JK., Landy, JC., Else, BGT., Campbell, K., & Papakyriakou, TN. (2018). The Energetics of Extensive Meltwater Flooding of Level Arctic Sea Ice. *Journal of Geophysical Research: Oceans*, *123*(12), 8730-8748. https://doi.org/10.1029/2018JC014045

Publisher's PDF, also known as Version of record

Link to published version (if available):
10.1029/2018JC014045

Link to publication record in Explore Bristol Research
PDF-document

This is the final published version of the article (version of record). It first appeared online via Wiley at https://agupubs.onlinelibrary.wiley.com/doi/10.1029/2018JC014045. Please refer to any applicable terms of use of the publisher.

University of Bristol - Explore Bristol Research
General rights

This document is made available in accordance with publisher policies. Please cite only the published version using the reference above. Full terms of use are available:
http://www.bristol.ac.uk/red/research-policy/pure/user-guides/ebr-terms/

Journal of Geophysical Research: Oceans

RESEARCH ARTICLE
10.1029/2018JC014045

The Energetics of Extensive Meltwater Flooding of Level Arctic Sea Ice

A. Diaz[1], J. K. Ehn[1], J. C. Landy[2], B. G. T. Else[3], K. Campbell[1], and T. N. Papakyriakou[1]

[1]Centre for Earth Observation Science, Riddell Faculty of Environment Earth and Resources, University of Manitoba, Winnipeg, Manitoba, Canada, [2]Bristol Glaciology Centre, School of Geographical Sciences, University of Bristol, Bristol, UK, [3]Department of Geography, University of Calgary, Calgary, Alberta, Canada

Key Points:
- Surface energy balance of landfast sea ice measured during a delayed but then rapid melt season transition
- The timing and effects of transient low-pressure weather systems were key to explain ice melt stages
- Formation of impermeable superimposed and interposed ice layers was crucial to extensive surface flooding

Supporting Information:
- Supporting Information S1
- Movie S1

Correspondence to:
A. Diaz,
umdiaza@myumanitoba.ca

Citation:
Diaz, A., Ehn, J. K., Landy, J. C., Else, B. G. T., Campbell, K., & Papakyriakou, T. N. (2018). The energetics of extensive meltwater flooding of level Arctic sea ice. *Journal of Geophysical Research: Oceans*, *123*, 8730–8748. https://doi.org/10.1029/2018JC014045

Received 4 APR 2018
Accepted 29 SEP 2018
Accepted article online 12 NOV 2018
Published online 5 DEC 2018

©2018. American Geophysical Union. All Rights Reserved.

Abstract During the spring-to-summer transition, the snow cover on Arctic sea ice melts and meltwater pools on the surface to form melt ponds; however, the timing and extent of the ponding vary between years. In Dease Strait (Nunavut), this transition was particularly dramatic in 2014 when on 18 June meltwater had flooded >95% of the surface. In this study, continuous surface energy balance measurements throughout the transition highlight how the timing of transient weather events influenced seasonal shifts in distinct ice melt stages. The keys to the extensive flooding were (1) the level ice cover, (2) a strong low-pressure system on 24 May that deposited ~10 cm of snow, and (3) freeze-thaw cycling and a subsequent return to subzero air temperatures on 30 May that led to superimposed and interposed ice formation. Without these, melt ponds would have likely developed within days from an initial melt onset on 28 May. After a 2-week delay, snow-melt resumed and lead to near-complete flooding of the surface for 4 days. The albedo of the flooded ice remained high (0.35–0.40), as a result of the bubble-laden superimposed ice layer. Once this layer eroded, the albedo over melt ponds decreased to a more typical level (~0.20). Our observations suggest that the formation of superimposed and interposed ice prevented the vertical drainage of meltwater to the ocean. Future challenges remain to measure the presence of these layers and understand their effect on sea ice permeability and pond evolution, while sea ice temperatures are near the melting point.

Plain Language Summary Melt ponds form on Arctic sea ice during the summer melt season, but the timing of their formation and extent varies from year to year. In June 2014 in Dease Strait (Nunavut), melt pond formation occurred later than usual and then caused near complete flooding of the ice surface. We conducted continuous surface energy balance measurements during this period. We observed a link between the occurrence of weather events, such as low-pressure systems, and changes to the sea ice melt progression. The extensive flooding of the ice surface with meltwater could be explained by (1) the flat ice cover, (2) the deposition of 10 cm of new snow and period of warm air temperatures associated with a southerly low-pressure system, and (3) a return to freezing conditions that led to widespread refreezing of snow meltwater s into ice layers at the sea ice-snow interface (superimposed ice) and within the upper part of the sea ice cover (interposed ice). This refrozen ice reduced the permeability of the ice cover and helped maintain melt ponds on the surface for longer. They also increased the albedo of the snow-free sea ice surface thereby playing a role in slowing the melt progression further.

1. Introduction

Impacts of global climate change are pronounced in the narrow waterways of the Canadian Arctic Archipelago (CAA), where feedback associated with the proximity of sea ice to land and the melt-growth cycle of sea ice are especially enhanced (e.g., Flato & Brown, 1996; Melling, 2002). This includes a reduction in the duration of the ice-covered season in the CAA, associated with trends toward earlier melt onset in spring-summer and later ice cover formation in fall (Galley et al., 2012; Stroeve et al., 2014). The waterways of the CAA are fully ice-covered for more than half of the year (Galley et al., 2012). Sea ice thus plays a key role in the CAA environment by regulating the exchange of momentum, heat, and gases between the atmosphere and the ocean; by limiting wind-driven mixing and waves; and by reducing light levels in the underlying water column. It provides a habitat for organisms from primary producers (Horner et al., 1992; Leu et al., 2015) to high trophic levels, such as ringed seals and polar bears. Its presence provides an essential platform for subsistence hunting by Inuit (e.g., Laidler et al., 2008) and is an important consideration in ever expanding travel through the Northwest Passage.

During the initial period of ice formation in the CAA, the thin ice cover is easily broken up by wind and waves into ice floes that may undergo ridging and rafting at their boundaries. Later, during calm and cold periods, the drifting ice floes consolidate into a solid immobile ice cover anchored to the coastline, termed landfast sea ice. The surface roughness elements created during early formation are important as they influence how snow is distributed on the ice (Iacozza & Barber, 2001). In turn, the snow cover exerts a significant control on the energy budget by effectively insulating the underlying sea ice from atmospheric temperatures (restricting ice growth in winter and ice melt in summer) and by increasing the surface albedo to >0.8 (Male & Granger, 1981; Nicolaus et al., 2003). Furthermore, recent work shows that the surface roughness of snow-covered landfast sea ice influences the spatial coverage of melt ponds formed during the summer melt period, which influences the timing of ice breakup (Landy et al., 2014, 2015).

During the winter to spring transition, the change from a negative (loss) to an increasingly positive (gain) in the sea ice energy budget leads to notable changes in the properties and physical state of the ice and overlying snow (Perovich et al., 2003; Persson, 2012). These changes have guided previous studies to identify distinct melt stages of the ice cover surface, which include premelt, melting snow, meltwater flooding, melt pond formation, and melt pond evolution (i.e., Eicken et al., 2002; Perovich et al., 2002; Persson, 2012). Inuit traditional knowledge has a deep understanding of these processes and melt stages, with well-developed terminology for communicating it in the Inuit language (Laidler et al., 2008). Variability in radiation forcing largely impacts the timing of transitions between melt stages of the ice cover (Mortin et al., 2016). This radiation forcing is affected by the presence of clouds, which can prompt warming or cooling of the surface (Intrieri et al., 2002). During premelt, a dry snowpack warms toward the freezing point, usually as a result of weather systems that reduce longwave losses (Else et al., 2014), increase in the down-directed turbulent heat fluxes, seasonal increases of incoming solar radiation, and/or a combination of these. However, the solar radiation may have a limited impact due to the high albedo of the snow at the premelt stage (Else et al., 2014). Melt onset is marked by melting of the surface snow and by a continuous increase in energy available within the snow cover, prompting further physical changes in the snowpack (Perovich et al., 2002). These changes include warm-process metamorphism (Colbeck, 1982), melting and refreezing (freeze-thaw cycle), thinning of the snow layer, and subsurface water saturation (Granskog et al., 2006; Haas et al., 2002). They directly feedback on the surface energy budget by decreasing the surface albedo and increasing absorption of solar radiation (Papakyriakou, 1999; Perovich et al., 2002). As the snow temperature reaches the melting point, diurnal freeze-thaw cycling becomes an important control of ice surface properties with melting occurring predominately during the day and refreezing of snow meltwater during the night (e.g., Ehn et al., 2006). Nicolaus et al. (2003) identified isothermal snow at the end of the diurnal freeze-thaw cycle as a melt onset marker condition.

The progression from melting snow to melt pond formation is closely linked to an increase in the energy available to the snowpack and a drop in the snow albedo (Perovich et al., 2002). The decrease in albedo leads to a positive albedo feedback by increasing the amount of energy available to melt snow and sea ice. Development of an impermeable layer at the snow/ice interface, known as superimposed ice, occurs as a result of meltwater percolation and refreezing when in contact with the colder ice surface (Kawamura et al., 2004; Koerner, 1970). Additional percolation and refreezing of meltwater can occur in the sea ice subsurface, which clogs sea ice channels and pockets to form interposed ice (Polashenski et al., 2017). These processes of refreezing meltwater have recently received scientific attention as they hinder meltwater from infiltrating into the underlying sea ice and thereby control the pooling and expansion of meltwater ponds over the surface (Polashenski et al., 2012, 2017). As the season advances, the capacity of the ice to retain meltwater on the surface will be controlled by the thawing of the impermeable layers (superimposed and interposed ice), the permeability of the underlying sea ice, and the development of macroscopic outflow pathways such as enlarged brine channels, cracks, and seal breathing holes (Eicken et al., 2002; Polashenski et al., 2012).

Of particular interest is the prediction of the timing of transition between stages in the melt progression identified above (Else et al., 2014; Nicolaus et al., 2003), their year-to-year variability, and how such transitions correlate with changes in the surface energy budget and the weather conditions that determine it. These transitions between melt stages are of importance as they influence the duration and intensity of sea ice growth and melt. These transitions, for both multiyear and seasonal sea ice covers, typically follow an irreversible seasonal progression (e.g., Else et al., 2014). It is important to understand the role of energy

budget components in promoting melt, the formation and deterioration of impermeable ice layers, and in particular the impact of their spatiotemporal variability and response to transient weather systems. Low-pressure weather systems can have a significant impact on the melt progression: for example, Else et al. (2014) showed that a single weather event (a 5-day cyclone) conveyed enough energy to accelerate snowpack warming and melt onset. It also stands to reason that certain transient weather events, and reversals in weather conditions, could slow down or reverse the progression of melt (e.g., Perovich et al., 2017). In a recent study by Perovich et al. (2017) the reversal of the seasonal melt progression was caused by a snowfall associated with a low-pressure weather system.

In this study we provide an example of a reversal in the ice surface melt progression linked to transient weather events. We present a time series of the full surface energy budget of the landfast sea ice cover in Dease Strait, Nunavut (Canada), over the spring to summer transition in 2014 during which the melting of snow and surface sea ice was interrupted by about 3 weeks and then commenced in dramatic fashion to briefly flood $>$95% of the surface. Captured in the time series is the impact of transient high- and low-pressure weather events on the energy budget and melt progression. In section 3, we present our observations of surface meteorology, snow and ice conditions, the conductive heat flux, and the surface energy fluxes. In section 4, the melt season stages are determined and their transitions are discussed, including the impacts of transient weather events and the formation of superimposed and interposed ice. The conclusions of the study are presented in section 5.

2. Materials and Methods

2.1. Study Area

The field observations (from 7 May to 26 June 2014) in Dease Strait (CAA) were conducted as a part of the Ice Covered Ecosystem-Cambridge Bay Process Study (ICE-CAMPS) 2014 field campaign operated out of Cambridge Bay, Nunavut (Figure 1). At the study site, located approximately 7 km offshore on landfast sea ice (69°01′48.6″N, 105°20′10.8″W), the sea ice surface was level, with a root-mean square roughness height of only 3.5 cm (Landy et al., 2015). The ice ranged from 1.7 to 2.0 m thick during the study period and was covered by up to 33 cm of snow. The ice and snow covers were observed to be void of significant sediment concentration. The water depth under the ice cover was 40 m. The study area was covered by snow until 17 June when melt ponds started forming rapidly. By 18 June, most of the snow had melted and the sea ice surface was covered by meltwater (see supporting information Movie S1). By this time, the land was mostly snow free. Refreezing and brightening of the ice was observed during night and the white ice surfaces became *crusty* and dry (Figure 1). By 20 June, meltwater channels radiating toward drainage holes (such as seal breathing holes, enlarged brine channels, or cracks) had formed in the sea ice in the study area. A sequence of photographs of the changes in the surface in the study area is shown in Figure 2.

2.2. Field Observations

A micrometeorological and flux tower (MET tower) was installed and operated in Dease Strait, Nunavut. The instrumentation on the MET tower (Figure 3) provided continuous measurements of meteorological elements and radiation fluxes. Site instrumentation included four component net radiometer (Kipp & Zonen model CNR4 with an integrated heater) mounted at 1.10 m (heights relative to the ice surface), an infrared transducer (Apogee SI-111, accuracy of ±0.5 °C) mounted at 1.68 m in height, a PAR sensor (Kipp & Zonen model PAR-Lite) mounted at 1.92 m, air temperature and relativity humidity probe (Vaisala HMP45C212, accuracy of ±0.1 °C) mounted at 2.11 m, an open path infrared gas analyzer (LI-COR, model LI-7500A, accuracy within 1% of CO_2 reading and 2% of H_2O reading) mounted at 2.03 m, a 3-D sonic anemometer (Campbell Scientific CSAT3, offset error $< \pm 8$ cm/s for u_x and u_y and $< \pm 4$ cm/s for u_z) mounted at 2.24 m, and a wind monitor (RM Young model 05106, accuracy of ±0.3 m/s) mounted at 3.05 m. Snow temperatures were measured at 3-cm intervals between the sea ice surface and 9 cm into the snow cover. Sea ice temperatures were monitored from the sea ice-snow interface to 1.80-m depth, about 3 m northeast of the tower, using a string of Type-T thermocouples. Seawater temperature was monitored at 2.40-m depth from the upper sea ice surface. All the above measurements with the exceptions of the 3-D sonic anemometer and the open path infrared gas analyzer, from 28 May onwards, were made at 1-s intervals, and 5-min averages were stored on the data logger (Campbell Scientific Model CR3000) with a multiplexer (Campbell Scientific Model AM 16/32B) used in conjunction with the thermocouples. Prior to 28 May, the

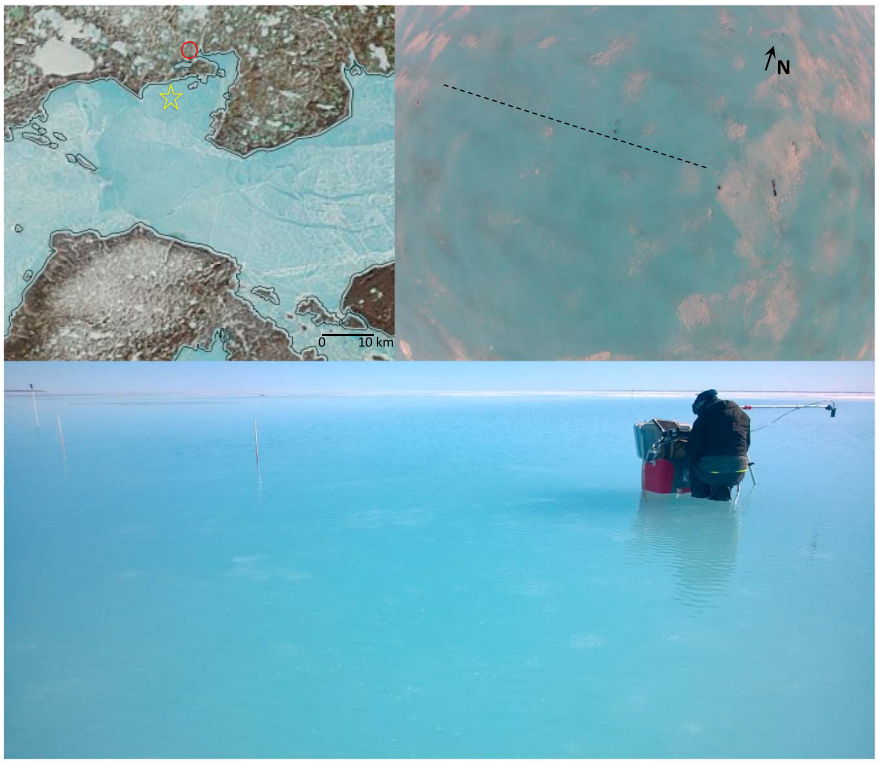

Figure 1. Location of the study area marked by a star; Cambridge Bay location marked by a circle. All images were taken on 21 June 2014. The top left panel shows a Moderate Resolution Imaging Spectroradiometer (MODIS) TrueColor satellite image (source: National Aeronautics and Space Administration [NASA] Worldview; https://worldview.earthdata.nasa.gov). The top right panel shows an aerial photograph (GoPro) of a 160-m albedo transect line (dotted line added to photograph). The lower panel shows a surface level view of the transect line with flooded (1- to 5-cm water depth) superimposed ice. The three main sea ice surface types observed in the aerial photograph are (i) exposed white ice elevated above the meltwater surface (bright areas), (ii) flooded bare ice (dark areas), and (iii) flooded superimposed ice (light blue areas). The dark adjacent land areas (MODIS image) indicate snow-free conditions.

data-recording and storage interval was set up at 2-s intervals. Eddy covariance measurements for turbulent heat fluxes (sensible and latent heat fluxes) were calculated (section 2.2 below) from high-frequency measurements (10 Hz) resulting from the 3-D sonic anemometer and the open path infrared gas analyzer. Daily visits to the site were made to ensure that the instruments were working and to prevent issues in the radiative measurements associated with leveling and/or condensation in the domes. Variations in the surface around the tower (snow drifts and variable melting) may have impacted the surface reflectance as the position of the Sun changes (Figure 3). The data set was augmented by spectral albedo measurements (350–2,500 nm) taken every 5 m along a transect line using a spectroradiometer (ASD FieldSpec Pro; Figure 1). The transect line was located approximately 2.5 km away from the tower.

Changes in snow depth were measured using two rulers frozen into the ice ~1.5 m away from the tower. Surface characteristics, environmental conditions, and cloud cover were documented daily through direct visual observations and photography. Stratigraphic profiles, temperature, salinity, and density of the snow cover were documented through snow pit observations. Samples and temperature measurements in the snow pits were collected in situ every 0.02 m using a snow kit sampling equipment and a temperature probe (Traceable Digital Thermometer, Control Company, accuracy of ±0.01 °C). Temperature measurements augmented those associated with the preinstalled thermocouple sensors identified above. Salinity and mass measurements of the snow samples were determined, after melting the samples at room temperature, with a hand-held conductivity probe (HACH SENSION5, accuracy of ±0.1 ppt) and an analytical balance, respectively. An ice core was collected approximately every 4 days over the sampling period, for assessment of ice thickness, temperature, and salinity. Measurements of sea ice salinity and temperature were made on defined sections of the ice profile, from the ocean water-ice interface to 5 cm and every 10 cm thereafter, with a

Figure 2. Sequence of images showing the transition to melt from 11 to 23 June. (a) Snow-covered ice image taken before melt onset, (b) beginning of pond formation, (c) maximum melt pond coverage at the study area, (d) meltwater draining laterally through opening in the sea ice, (e) drained white ice and melt pond, and (f) fully developed drainage network.

hand-held temperature probe (Testo 720 probe, accuracy of ±0.2 °C), and a conductivity probe (Orion Star A212 conductivity bench top meter, accuracy of 0.5% of reading ±1 digit), respectively. Immediately after removing an ice core, the temperature measurements were obtained by drilling into the center of the ice sections and inserting the temperature probe through the drilled hole into the ice. A second ice core was extracted and cut into defined vertical segments. Vertical segments were transported to laboratory facilities and were melted at room temperature to ascertain profiles of bulk ice salinity. Temperature and pressure record immediately beneath the sea ice (temperature accuracy of ±0.1 °C and resolution of 0.01 °C; pressure accuracy of 0.5% and resolution of 0.005% of full scale), and underice water current profiles were measured at 10-min intervals using a downward facing acoustic Doppler current profiler (Aquadopp 600 kHz z-cell, Nortek AS, accuracy of 1% of measured value ±0.5 cm/s) fixed to the ice cover about 200 m away from the tower. Seawater salinity measurements were obtained from a conductivity, temperature, and pressure (depth) logger (RBR XR-620 CTD, accuracy of ±0.003 mS/cm, ±0.002 °C, and ±0.05% full scale for conductivity, temperature, and depth readings, respectively).

2.3. Calculations of Energy Budget

Net atmospheric energy flux to the surface is formulated as follows

$$F_{\text{net}} = Q^* - Q_E - Q_H, \tag{1}$$

where

$$\begin{aligned} Q^* &= K^* + L^*, \\ &= K_{\text{in}}\text{-}K_{\text{out}} + L_{\text{in}} = L_{\text{out}}, \end{aligned} \tag{2}$$

where Q^* is net all wave radiation and Q_E and Q_H, are the latent heat flux and sensible heat flux. K and L denote shortwave radiation and longwave radiation, respectively, with the subscripts *in* and *out* and the superscript asterisk referring to incoming (downwelling), outgoing (upwelling), and net-all wave values,

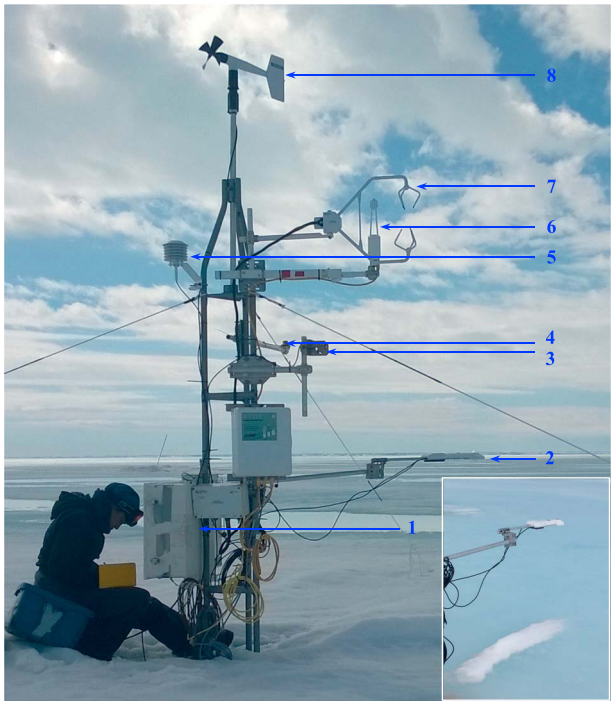

Figure 3. Micrometeorological and flux tower located at 69°01′48.6″N 105°20′10.8″W on land fast sea ice in Dease Strait. Instruments housed on the tower: (1) CR3000 data logger and AM16/32B multiplexer housed in an insulated enclosure, (2) CNR4, (3) infrared transducer, (4) PAR, (5) air temperature and relative humidity probe, (6) open path infrared gas analyzer, (7) 3-D sonic anemometer, and (8) wind monitor. The lower right panel corresponds to an image of the area under the CNR4 taken on 18 June depicting the no fully homogenous surface around the tower.

respectively (Oke, 1987). A positive/negative F_{net} indicates a net gain/loss in energy from/to the atmosphere. Downwelling radiative terms (K and L) represent gains of energy by the surface and upwelling terms energy losses. Radiative fluxes (K_{in}, K_{out}, L_{in}, and L_{out}) were directly measured by the CNR4 housed on the tower (Figure 3). These fluxes (K_{in}, K_{out}, L_{in}, and L_{out}) were visually prescreened to identify whether sudden fluctuations in the 24-hr incoming shortwave radiation were produced by clouds or were an obstruction shadow (see Figure S1 in the supporting information). By plotting the daily radiative energy fluxes, time intervals in which an obstruction shadow was identified and these data points were replaced with NaN (i.e., *not a number* in MATLAB).

Turbulent heat fluxes (Q_E and Q_H) are positive when they represent losses of energy for the surface (up-directed flux) and negative when they represent gain of energy at the surface (down-directed flux). The eddy covariance method was used to calculate the these fluxes, as follows

$$Q_E = L\overline{\rho_v{}'w'} \tag{3}$$

and

$$Q_H = \rho_a c_p \overline{w'\theta'}, \tag{4}$$

where L, ρ_v, ρ_a, c_p, w, and θ denote latent heat, water vapor density, air density, specific heat capacity of air, vertical wind speed, and air temperature, respectively. The prime denotes instantaneous fluctuation in the respective terms (ρ_v', w', and θ'), and the over bar indicates the time average of the covariance terms ($\rho_v' w'$, and $w'\theta'$). These parameters were obtained from the open path infrared gas analyzer and 3-D sonic anemometer housed on the tower (Figure 3). The Q_E and Q_H are subject to approximately ±15% uncertainty (Leuning et al., 2012). The turbulent heat fluxes were computed for 20-min sampling periods and visually prescreened to remove inconsistent values such as large sporadic negative and/or positive outliers in the data (see Figure S1). Outlier points were replaced by NaN.

In the full surface energy balance equation for a snow/ice volume, F_{net} is balanced by subsurface terms:

$$F_{net} = G + \Delta Q_s, \tag{5}$$

where G is the conductive heat flux to the surface and ΔQ_s represents a storage term that accounts for energy absorption or release in the underlying snow, ice, and water volume (Oke, 1987). In this study, with highly variable and changing snow and ice conditions (see section 2.1 for a description of the study area), we do not attempt an estimate of transmitted solar radiation (e.g., Else et al., 2014; Persson, 2012), which is required for a calculation of the energy balance of the snow and/or sea ice volume. Instead, G is presented separately to show the direction of energy fluxes in the snow and ice. The net atmospheric flux (F_{net}) magnitudes were observed to be an order of magnitude larger than the conductive heat flux (G), indicating the dominance of internal changes associated with warming/cooling, and melting/freezing.

The conductive heat fluxes in the snow cover (G_s) and sea ice (G_{si}) were calculated as follows:

$$G_s = -\kappa_s (T_{surf} - T_{interf})/(z_{surf} - z_{interf}), \tag{6}$$

for the snow cover, and

$$G_{si(upper)} = -\kappa_{si} (T_{interf} - T_n)/(z_{interface} - z_n), \tag{7}$$

and

$$G_{si(lower)} = -\kappa_{si} (T_n - T_{bottom})/(z_n - z_{bottom}), \tag{8}$$

where κ_s is the thermal conductivity, T is absolute temperature (K), and z is depth; the subscripts s, si, surf, interf, bottom, and n denote snow, sea ice, surface, snow-sea ice interface, sea ice bottom, and sea ice

middepth, respectively. Positive conductive heat flux indicates downward flux and negative conductive heat flux upward flux. T_{interf}, T_n, and T_{bottom} were obtained from the thermocouple string. The depth of T_n was selected based on observed changes in the vertical profiles of temperature and salinity of the sea ice. Surface skin temperature, T_{surf}, was collected by infrared transducer (Figure 3). Following the deployment of the instruments at the beginning of the experiment, the infrared transducer did not record the surface temperature during some periods due to connectivity issues. During periods of missing surface temperature, this parameter was estimated using

$$T_{surf} = (L_{out}/\varepsilon\sigma)^{1/4} \tag{9}$$

adopting a surface emissivity (ε) of 0.985 (Persson, 2012) and Stefan-Boltzmann constant (σ) of $5.67 \times 10^{-8} \cdot \mathrm{Wm}^{-2} \cdot \mathrm{K}^{-4}$. Snow thermal conductivity, κ_s, and sea ice thermal conductivity, κ_{si}, were estimated respectively following Sturm et al. (1997) and Pringle et al. (2007):

$$\kappa_s = 0.138 - 1.010\times10^4\rho_s + 3.233\times10^6\,\rho_s^2 \;(150 \leq \rho_s < 8,600\ \mathrm{kg/m3}) \tag{10}$$

and

$$\kappa_{si} = {}^{\rho_{si}}/_{\rho_i}(2.11 - 0.011T + 0.09S_{si}/T_{si} - (\rho_{si} - \rho_i)/1,000), \tag{11}$$

where ρ denote density and the subscript i denotes pure ice. S_{si} and T_{si} were obtained from sea ice cores and thermocouple strings. The ρ_{si} was estimated after calculating sea ice volume fractions using S_{si} and T_{si} (Cox & Weeks, 1983; Leppäranta & Manninen, 1988). The ρ_s was computed from mass and volume data obtained from the snow samples. Snow density, snow depth, sea ice thickness, sea ice salinity, and sea ice density measurements used to estimate the conductive heat flux were interpolated linearly to have the same temporal resolution as the meteorological parameters and the radiative and turbulent heat fluxes.

In addition to these parameters, the daily cloud radiative forcing (CRF) was calculated following Intrieri et al. (2002) approach as follows

$$\mathrm{CRF} = Q^* - Q^*_{CS} \tag{12}$$

where

$$Q^*_{CS} = K_{in\_CS} - K_{out\_CS} + L_{in_{CS}} - L_{out\_CS}, \tag{13}$$

where $Q^*_{CS}, K_{inCS}, K_{outCS}, L_{inCS}$, and L_{out_CS} denote the expected local net radiation and downwelling and upwelling shortwave and longwave radiation fluxes under clear sky. A linear regression model obtained using the direct measurements of K_{in} and L_{in} for clear-sky days during the study period was used to calculate the expected radiative fluxes. When clouds are prompting warming of the surface, CRF is positive (+CRF). Negative cloud radiative forcing (−CRF) indicates cooling.

3. Results

3.1. Weather Conditions

Temperature exhibited an overall increase superimposed by relatively large daily variability (Figure 4). Pronounced variability was also observed in atmospheric pressure and wind speed, as well as cloud cover (not shown), as is typical for the winter to summer seasonal transition in the CAA (Else et al., 2014; Papakyriakou, 1999; Stroeve et al., 2014). Five distinct, but relatively brief, warming events were observed between the start of the experiment and 30 May, and these were centered on 14, 18, 24, 26, and 28–29 May (Figure 4b). During these events air temperature exceeded 0 °C and surface temperature approached the melting temperature (Figure 4). Notably, the warming events developed concurrently with the passage of low-pressure systems from the southwest (see Figures S2 and S3); a correlation analysis of the surface temperature and pressure yields an inverse correlation ($r = -0.73$). Upon the approach of these low-pressure systems, the site was typically located in the warm side of the storm with its southerly flow of air and high wind speeds (Figure 4). The more pronounced of the low-pressure systems (99.15 kPa) brought significant snowfall and high winds on 24 May (Figure 4a; see Figure S3 for details in the movement of this low-pressure systems). Northerly advection of air over the period between 30 May and 12 June, associated with a high-pressure system, resulted in subfreezing air temperature, following thereafter by above zero temperature through to the

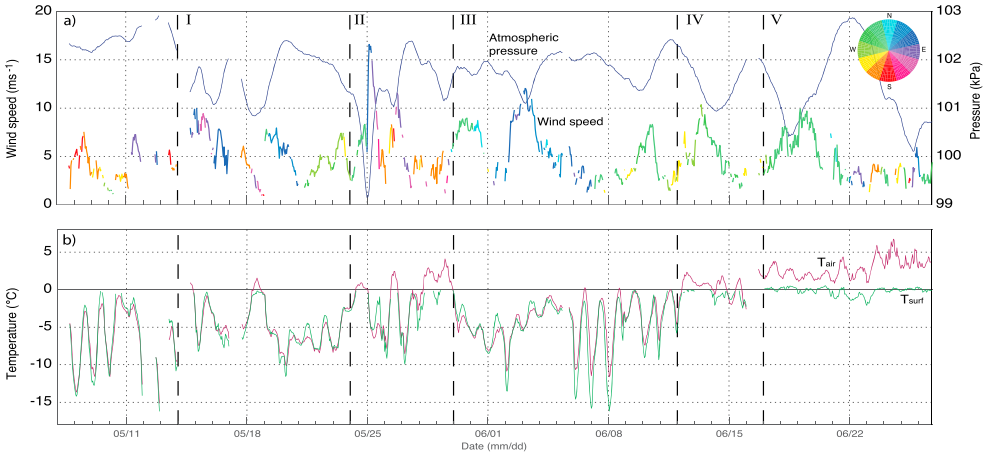

Figure 4. Time series of hourly means of (a) wind speed (m/s), wind direction (°), and atmospheric pressure (kPa), and (b) air temperature (T_{air}, °C) and surface temperature (T_{surf}, °C) in local solar time. The vertical dashed lines mark seasonal transitions of the ice surface: (I) spring transition, (II) snowfall event, (III) melt hiatus, (IV) snowmelt onset, and (V) pond formation.

end of the experiment. The return to subfreezing air temperature was followed by additional snowfall occurring on 1 June and then 3 days (3–5 June) of predominantly cloudy conditions with intermittent light snowfall. Relatively minor precipitation events brought by the passage of low-pressure systems occurred on 9 June (light snow fall) and 13 June (ice pellets, rain, and snow showers; Figure 4). The transitions marked with Roman numerals in Figure 4 are discussed in section 4.

3.2. Snow and Ice Core Observations

The stratigraphic sequence of the snow profiles encompassed layers of fresh/new snow, bulk snow, depth hoar, and ice layers (Figure 5). These layers varied in thickness from 1 to 16 cm. The bulk density of the snow profiles varied from 281 to 479 kg/m^3. The ice layers included internal ice lenses and superimposed ice at the snow-ice interface. Between 1 and 9 June, superimposed ice was observed at various locations in the study area. By 16 June, the snow cover was saturated and the superimposed ice had, then, decreased by approximately 2 cm from 9 June.

Ice core observations showed that the upper layer of the sea ice cover began to freshen between 30 May and 5 June (Figure 6) even though air temperature remained below freezing (Figure 4b). Over the 30 May to 5 June period, we observed a drop in the brine volume in layers above the depth of 10 cm by about 65%

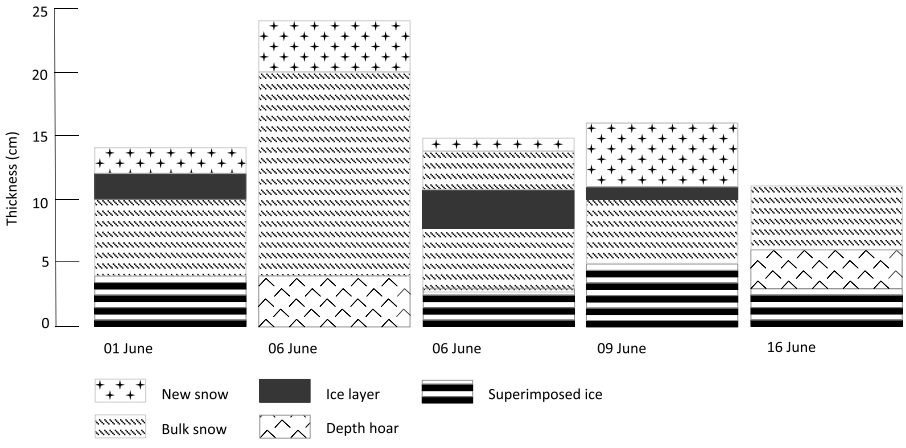

Figure 5. Selected snow stratigraphic profiles from snow pits suggest changes in the snow cover from 1 to 16 June. Water-saturated snow profile documented on 16 June.

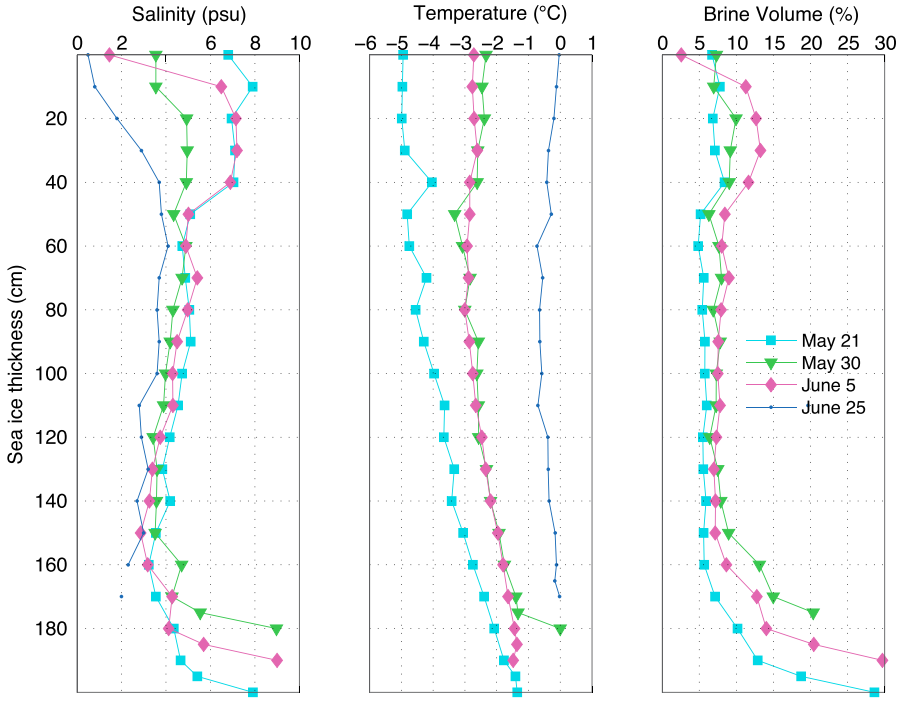

Figure 6. Vertical profiles of bulk salinity, temperature, and brine volume fraction in sea ice. Ice cores obtained at adjacent sites. Relative volume of brine on 25 June (>20%) was not included.

accompanied by about 40% increase in the brine volume between 10- and 40-cm depth; by comparison, the temperature of sea ice was relatively constant in these upper layers. Salinity profiles 40 cm below the ice surface toward the bottom showed a decrease in salinity with depth and time from 21 May onward. By contrast, brine volume was relatively constant with depth down to ~140 cm and increased slightly over time. Higher levels of salinity and brine volume were present near the bottom (i.e., below 150-cm depth) in all of the ice cores. By 25 June, the ice cover had freshened down to salinities less than 4 psu suggesting a minimum brine volume of about 20%.

3.3. Conductive Heating in the Sea Ice and Snow

The conductive heat flux in the snow (G_s) showed pronounced variability in response to radiative warming by day and cooling at night (Figure 7c). This diurnal variation was most pronounced during cold periods such as from 7 to 11 May. When the snowpack warmed, for example from 28 to 31 May, the temperature gradient reversed, leading to a decrease in the temperature gradient in the upper portion of sea ice (40 cm down from the snow-sea ice interface) and then later a reversal. During these periods the snowpack gradually moves toward isothermallity. G_s, then, became a source of energy to the underlying sea ice.

Until 14 May, $G_{si(upper)}$ displayed diurnal changes in direction closely matching G_s, transferring heat upward to the overlying snowpack at night (except on 11 May) and downward during daytime (Figure 7c). The close match in conductive heat fluxes suggests that latent heating associated with phase transformations (i.e., melting/freezing) in the upper ice cover were modest. From 14 May onward, the heat transfer in the upper section of sea ice, $G_{si(upper)}$, was mostly directed downward from the snow-ice interface toward the cold midsection of the sea ice, which gradually warmed over the study period. The lower section of sea ice (from the 40-cm depth to the bottom of sea ice) was characterized by a typical upward conductive heat flux, $G_{si(lower)}$, without the diurnal variability seen near the surface. The upward flux suggests ice growth. The heat flux in this zone decreased over the course of the study period in response to overall warming of the sea ice. Hence, after 14 May, both $G_{si(upper)}$ and $G_{si(lower)}$ warmed the interior of the ice.

Pressure from the acoustic current profiler installed under the ice cover that was fixed (frozen) to the ice cover provided a means to track the isostatic movement of the sea ice cover relative to the sea level (Figure 7d)

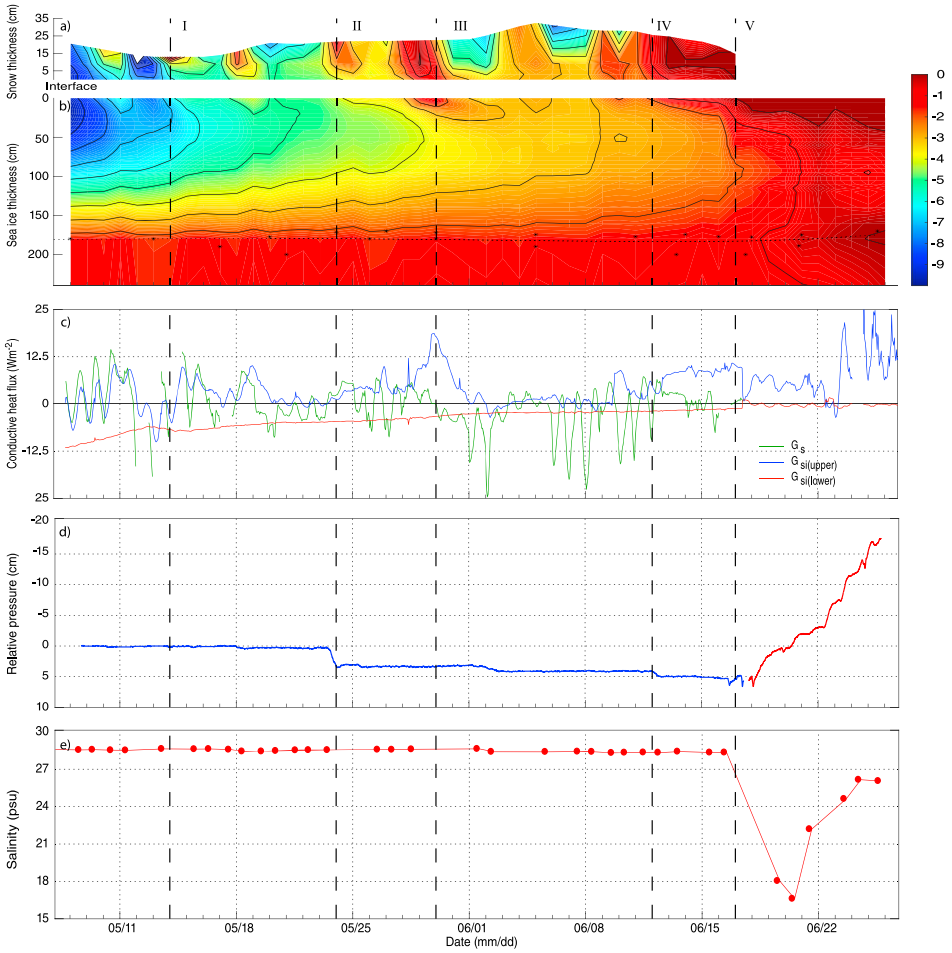

Figure 7. Time series of (a) daily mean vertical temperature (°C) in snow, (b) daily mean vertical temperature (°C) in sea ice and seawater, (c) hourly means of conductive heat fluxes (W/m^2), (d) relative pressure (cm) indicating isostatic movement of the ice cover relative to the sea level, and (e) average seawater salinity from 1.80 to 2.20 m in local solar time. Ice thickness (*) measurements were obtained from ice core samples at adjacent sites. Snow thickness measurements obtained from rulers frozen into the ice ~1.5 m away from the MET tower in the study site. The horizontal dashed line in (b) indicates ice thickness trend line.

after correcting for atmospheric pressure. Underice pressure remained relatively steady until 24 May when the snow loading, associated with the low-pressure system, depressed the ice cover by ~4 cm. Steady conditions resumed until full melt on 17 June, with only two smaller precipitation events evidenced by a 1-cm pressure increase on 1 June and <1-cm increase on 12 June. Measurements suggest that there was not significant change to the sea ice mass through thermodynamics. On 17 June, a melt hole formed at the current profiler installation, and it had to be relocated to a nearby more elevated site where it consequently refroze into the ice. From 17 June onwards, a continual rise of the ice cover relative to the sea level is evidenced by the pressure decrease at an average rate of 2.8 cm/day (red curve in Figure 7d). By 19 June the ice cover rebounded to the pre-24 May level (Figure 7d). The average salinity of the seawater at 2-m depth (Figure 7e) remained relatively constant at 28.5 until 17 June, whereafter values rapidly decreased in response to underice flooding to the lowest recorded value of 16.5 on 20 June.

3.4. Surface Energy Fluxes

The 4-hourly-averaged turbulent heat fluxes (sensible, Q_H, and latent, Q_E) showed day-to-day variability, varying between 46 to and 34 W/m^2 for sensible heat, and 44 to −46 W/m^2 for latent heat (Figure 8). Q_H was typically up-directed during daytime between 9:00 and 16:00 (local solar time) and down-directed between 16:00 and 9:00 (Figure 8a). However, Q_E and Q_H mostly down directed energy to the surface during the warm periods with strong surface melting such as from 28 to 30 May and from 17 June onward. Incoming

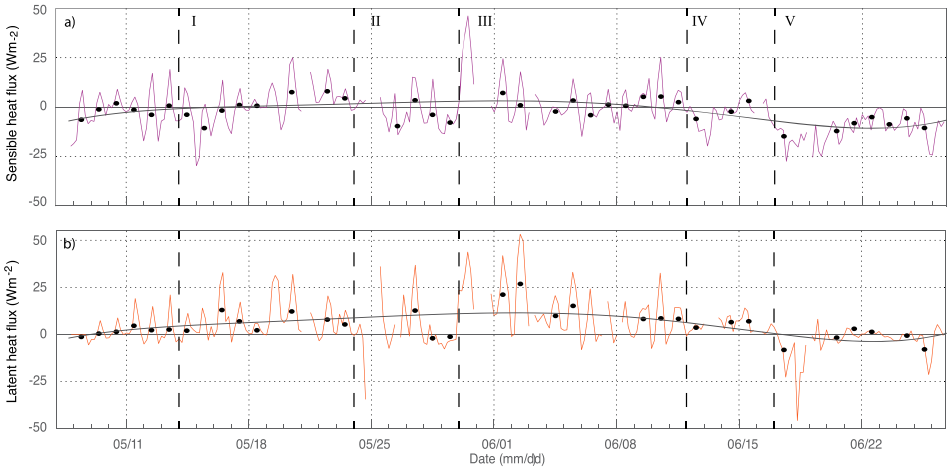

Figure 8. Time series of 4-hr averages of turbulent heat fluxes (W/m^2). (a) Sensible heat flux (Q_H); (b) latent heat flux (Q_E) in local solar time. Positive values represent up-directed flux (energy loss from the surface); negative values indicate down-directed flux (energy gain at the surface). Polynomial curve fitting of Q_H and Q_E show as black solid lines in plots a and b, respectively. The black circles correspond to 24-hr mean.

and outgoing shortwave radiation (K_{in} and K_{out}) closely mirrored each other until 17 June (Figure 9a) in response to a rapid and pronounced drop in surface albedo, coinciding with the disappearance of the snow cover and appearance of meltwater on the ice surface. During overcast conditions, emitted and received longwave radiation (L_{out} and L_{in}) were closely matched (Figure 9b), resulting in small net longwave radiation loss from the surface, particularly for the periods 9–12 May, 18–26 May, 2–5 June, 11–14 June, and 17–20 June. Temporal and spatial variability in surface albedo was observed, responding to changes in snow surface (melt-freeze cycles at the surface; Figures 9a and 10). Surface albedo measurements show that albedo dramatically decreased between 14 and 17 June (Figures 9a and 10), then again progressively decreased on 21 and 23 June. Albedo ranged from 0.21 to 0.25 along the 21 June transect. Overall, the albedo had decreased by about 0.15 from 17 to 23 June (Figure 10).

Net radiation (Q^*) was positive over most of the study, while particularly large fluxes were observed during clear sky conditions and linked to large daytime net solar radiation (K^*), as shown for example on 8 May and 21 June, and to large daytime net solar radiation (K^*) and low longwave radiation loss, as shown for

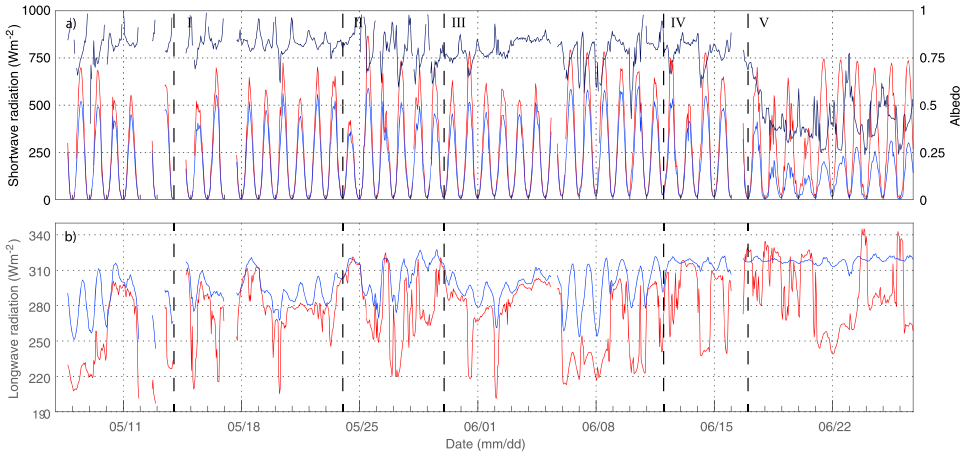

Figure 9. Time series of hourly means of radiative energy fluxes (W/m^2) in local solar time: Downwelling radiative fluxes (red lines) indicate energy gain and upwelling radiative fluxes (blue lines) indicate energy loss; (a) downwelling shortwave radiation (K_{in}), upwelling shortwave radiation (K_{out}), and albedo (α, dark blue line); (b) downwelling longwave radiation (L_{in}), and upwelling longwave radiation (L_{out}).

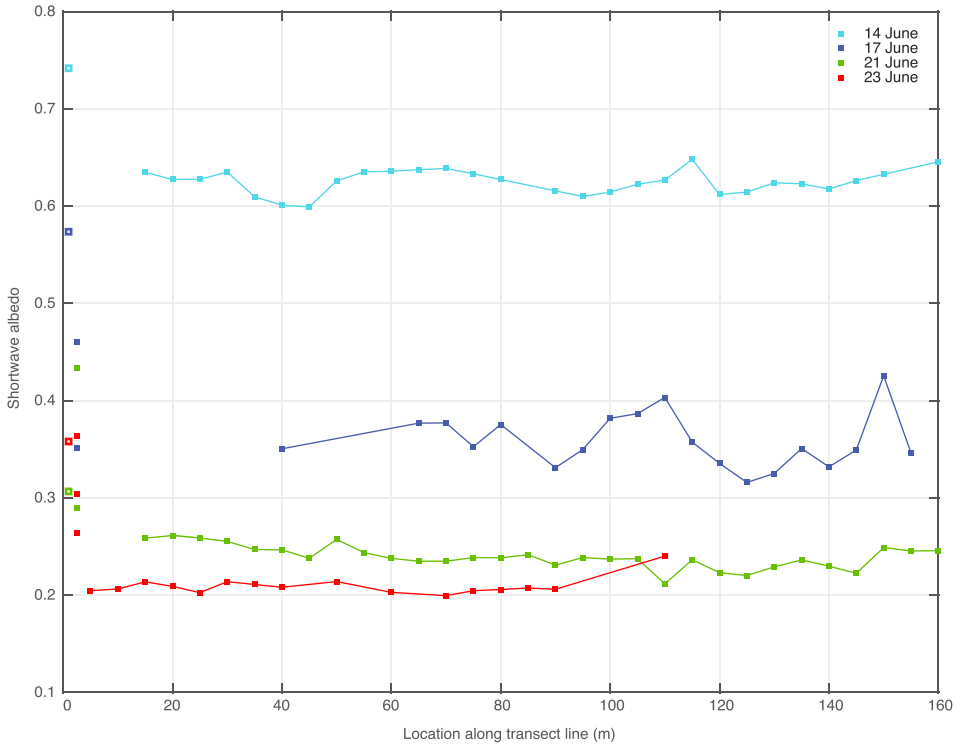

Figure 10. Albedo transect line west to east. Wet snow and clear sky for 14 June measurements taken between 13:30 and 15:01, slushy snow and ponds under variable cloud cover for 17 June measurements taken between 13:30 and 16:45, ponds with white ice and blue ice at the ponds' base under clear sky for 21 June measurements taken between 14:20 and 16:20, and mixed drained and wet ponds with mostly blue ice at the ponds' base under clear sky with some high clouds for 23 June measurements taken between 11:55 and 13:35. Points collated near *y* axis: the filled squares represent point measurement taken on exposed bare white ice (red and green squares) and slushy snow (blue squares) in areas immediately outside of the transect line, and the empty squares are the means of the measurements taken by the CNR4 housed at the MET tower during the same time intervals of the albedo transect measurements.

example on 25 May and 12 June (Figure 11). CRF was mainly positive during the study time; however, periods of negative cloud forcing were observed to occur more frequent after 17 June (Figure 11a). Mirroring trends observed for net radiation (Q^*), net atmospheric energy flux (F_{net}) alternated between daytime highs that ranged between 37 and 500 Wm^{-2} to nighttime losses of between −3 to −70 Wm^{-2} (Figure 11). During periods of low longwave radiation loss, minimum net atmospheric energy flux ($-F_{net}$) remained close to 0 (Figure 11). The daytime peak net atmospheric energy flux ($+F_{net}$) suddenly increased 280 W/m^2 from 17 to 22 June (Figure 11).

4. Discussion

4.1. Important Episodes in the Transition to Advanced Melt

In this study, we report on a melt season transition from cold snow-covered sea ice to a nearly fully flooded surface. A key factor was the passage of low-pressure systems, which brought in warm and cloudy air masses (Figure 4). These transient events marked distinct transitions between periods within which we observed relative uniformity in energy budget terms and unchanging surface conditions. In the following we discuss five important transitions that underpinned the evolution toward the onset and progression of melt (identified with Roman numerals in Figure 4, from Figures 7 to 9 and 11): (I) spring transition, (II) snowfall event, (III) return to winter conditions (melt hiatus), (IV) melt onset, and (V) melt pond formation (see Table S1 in the supporting information for the integrated values of the energy flux terms over the periods between these transitions).

4.1.1. Conditions Leading to Initial Melt Onset (Until 30 May)

Two distinct transitions (I and II in Figures 4, 7, 8, 9, and 11) that significantly contributed to warming and ultimately to the timing of initial melt onset observed on 28 May were linked with the arrival of low-

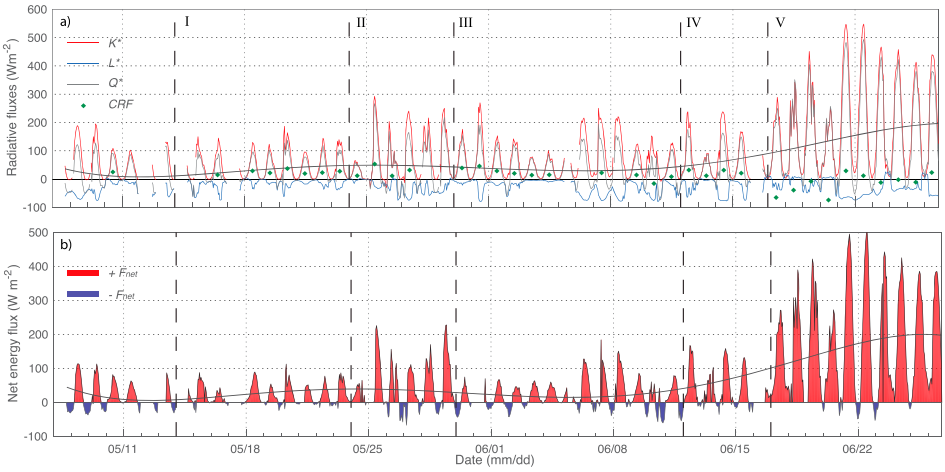

Figure 11. Time series of (a) hourly means of net shortwave radiation ($K^* = K_{in} - K_{out}$), net longwave radiation ($L^* = L_{in} - L_{out}$), net radiation ($Q^* = K^* + L^*$), and daily means of cloud radiative forcing (CRF $= Q^* - Q^*_{CS}$); (b) hourly means of net atmospheric energy flux ($F_{net} = Q^* - Q_H - Q_E$) in local solar time. Positive net atmospheric flux ($+F_{net}$) indicates a gain, and negative ($-F_{net}$) indicates a loss. Polynomial curve fitting of Q^* and F_{net} shown as black solid lines in plots a and b, respectively.

pressure systems. Transition I occurred on 14 May during which time both air temperature (T_{air}) and surface temperature (T_{surf}) reached 0 °C for the first time during the observation period (Figure 4). Transition II occurred on 24 May when another low-pressure system, arriving from the southwest (Figure 4a), brought a significant snowfall (~13 cm), above freezing air temperature and strongly positive net atmospheric energy flux (Figures 4b and 11), largely through effect of the warm air mass and cloud cover on the longwave exchange (Figures 9 and 11). We measured an increase in snow thickness of only 1 to 2.6 cm at the MET tower; however, an isostatic depression of the ice cover of approximately 4 cm that was recorded by the underice current meter (Figure 7d) suggests approximately 13 cm of new snow near to the site, assuming ice and new snow densities of 900 and 300 kg/m^3, respectively. This estimate is very close to the 13.5 cm of snow recorded at the nearby Environment and Climate Change Canada weather station in Cambridge Bay between 25 and 26 May, and consequently, snow depth measured in proximity to the ruler at the station was likely affected by the redistribution of snow by wind. The new snow acted as a heat sink providing a better insulation for the underlying snow and sea ice and increased the surface albedo limiting the absorption of downwelling shortwave radiation (Perovich et al., 2017). This new snow would constitute water supply for melt ponds.

Three short-lived increases in the surface temperature (Figures 4b and 7a) between 14 and 24 May were associated with a sequence of low-pressure systems that produced a period of warm-air advection and, thus, clouds enhancing downwelling longwave radiation and down-directed sensible heat flux (Figures 4, 9, and 11). The effect of clouds on the longwave exchange was to maintain net radiation loss ($-Q^*$) close to 0, thereby aiding the warming of the surface (+CRF) and restricting nocturnal radiation loss and associated refreezing at night (Figure 11). Previous studies suggest that the cloud effect may be an important contributing factor in promoting melt onset (Ehn et al., 2006; Else et al., 2014; Mortin et al., 2016; Papakyriakou, 1999; Persson, 2012). In fact, cloudy periods have been described as a controlling factor of the warm-up period preceding melt onset (Else et al., 2014).

With the arrival of the cold sector following passage of the most pronounced low-pressure system, the air temperature dropped rapidly from 0 to −6.5 °C by the end of 25 May (Figure 4b). It is evident that the combination of cold air and new snow briefly interrupted the progression of temperature waves and, thus, the surface melting and warming of the snowpack. By 27 May, however, warm air and overcast conditions supported both down-directed sensible heating (Figure 8a) and a rise in net radiation (Figure 11). Subsequently, the onset of melt occurred on 28 May when T_{air} and T_{surf} approached 0 °C with the snowpack having approached isothermal temperature profile (Figure 7a). Melting of the snow initiated releasing meltwater in response to consecutive days of positive daytime net radiation (Figure 11) and prompted an initial

lowering of 24-hr minimum albedo below early season values (Figure 9a). The ensuing temperature waves and downward conductive heat flux associated with the warm air temperatures on 24 May and 28–29 May were observed to cause partial melting of the snow cover and the near-surface portion of the sea ice, consequently increasing the snow-sea ice interface temperature to approximately −0.5 °C and reducing the temperature gradient between snow and sea ice (Figure 7ab). Day-to-night fluctuations in the net atmospheric energy flux (Figure 11) resulted in freeze-thaw cycles, leading to the formation of ice lenses in the snowpack and superimposed ice at the snow-ice interface. The latter has been identified as a melt onset indicator in previous studies (i.e., Granskog et al., 2006; Nicolaus et al., 2003).

Past studies suggest that melt onset is typically irreversible and triggered by changes in snow properties brought on by melting (e.g., Else et al., 2014; Perovich & Polashenski, 2012). However, cycles of daytime thaw/nighttime freeze ended on 30 May with the return to subzero temperatures brought by the advection of cold air with winds from the north associated with a high-pressure system (Figure 4a). This marks transition III. More recent work shows that a transient weather event occurring when both net radiation and net longwave fluxes are positive can effectively interrupt the progression of melt (Perovich et al., 2017). Had the warming trend observed continued, melt pond formation would most likely have occurred within days, as was the case in Else et al. (2014).

4.1.2. Conditions Leading to Pond Formation (30 May to 17 June)

The shift to subzero air temperature and periods of high wind speeds (up to 12 m/s) following transition III caused snow to drift between 30 May to 5 June (Figures 4 and 7a). The snow cover thickness at the MET station increased from 22 to 33 cm by 5 June (Figure 7a) in response to new precipitation (1 and 3–5 June; Figure 7d) and redistribution of existing snow. Over the period, we observed decrease in net shortwave radiation (K^*) and net longwave radiation (L^*) loss resulting in overall positive but lower net radiation flux compared to the one observed preceding 30 May (Figures 9 and 11); cloud forcing remained positive yet its thermal effect on the surface decreased (Figure 11). Sea ice temperatures increased slowly throughout the cold phase (30 May to 12 June), attributed to the combination of the insulating effect of the thicker snow cover and oceanic heat flux at the ice base (Figures 6 and 7a–7c). Low-pressure systems at this time advected cooler air (see Figure S2).

Active melting of the snow started again on 12 June (transition IV) triggered by increase in net energy flux (F_{net}; Figure 11) and the return of above freezing air temperatures (Figure 4b) and positive cloud forcing (Figure 11) upon the approach of a low-pressure system (Figure 4a). The increase in the available energy resulted from low net longwave radiation loss (L^*; Figure 11), drop in the 24-hr minimum albedo (Figure 9a) and down-directed sensible heat flux (Figure 8) that allowed the snow again to become isothermal near to 0 °C (Figure 7). At this time, the precipitation event (ice pellets, rain, and snow showers) associated with the low-pressure system likely provided a small contribution to the snow warming by giving up sensible heat when in contact with the relatively colder snowpack. By 16 June, a *wet* snow cover, characterized by the continuous presence of meltwater in the snowpack, aided the system to transition into a period of melt pond formation (marked by transition V) by reducing the albedo and increasing the absorption of shortwave radiation (Figure 9). The formation of melt ponds was primarily triggered by the sustained isothermality of the snowpack for 5 days, increase in the amount of energy available linked to the enhanced albedo feedback, and the seasonal warming. The prefrontal warm air advection of a low-pressure system advancing toward the study zone (Figures 4 and S2) aided the melting and evolution of melt ponds. If the low-pressure system had come from the northwest or northeast (e.g., 3 and 9 June), it is likely that the advection of warm air had been less significantly precluding the evolution of melting.

4.1.3. Conditions Prompting the Evolution of Melt Ponds (From 17 June)

The combination of positive air temperature (Figure 4b), large positive net radiation (Q*; Figure 11), and down-directed turbulent heat fluxes (Figure 8) fuelled melt from 17 June onwards, and the surface evolved rapidly from a melting snowpack to near-complete flooding by 18 June (Figures 2a–2c). The dramatic decrease in the surface albedo on 17 June evidenced this change, having decreased from >0.7 to 0.3 on the morning of 18 June (Figure 9a), and helped to prevent the system to return to the relatively low net radiation and net atmospheric energy flux values observed preflooding (Figure 11). When clouds occurred (e.g., 20 June), they acted to cool the surface by lessening the amount of downwelling shortwave radiation reaching the surface (−CRF; Figure 11). Melt pond coverage was estimated to have been 95–100% in the flooded study area by 18 June (Figure 2 and Movie S1). Over this period Landy et al. (2015), indicated that

roughly 0.08 m meltwater per unit area were required to cover the observed topography (root-mean-square height of 0.035 m) by >95%, provided the ice was impermeable to vertical drainage. A 22-cm-deep snowpack with an assumed mean density of 438 kg/m^3 (as observed in a snow pit on 16 June) would account for a 0.096 m meltwater layer, although melting of the sea ice surface may have been additionally taking place. Rapid transitions like this are characteristic of melt pond evolution stage 1 described by Eicken et al. (2002).

Initially, horizontal surface flow was notable with the draining of meltwater through cracks and holes in the ice (Figure 2d). The continuous loss of mass from the ice surface from 19 June onward, as evidenced by the change in the relative underice pressure from the ice-tethered current meter (Figure 7d), is consistent with increase in surface melt rates expected from the loss of flooded superimposed ice that reduced the albedo (Figure 10) and the large net energy flux values (Figure 11). Positive air temperature (Figure 4) enhanced this melting of the ice by enhancing the down-directed sensible heat flux (Figure 8). The observed stepwise uplift of the ice cover is linked to the melt supply availability controlled by the diurnal cycling and the development of drainage channels. As the ice became isothermal, the daily variation in the available energy was used to melt the ice surface rather than increment its temperature. Persson (2012) noted that when the ice/snow surface reached its freezing point, the upwelling longwave radiation, turbulent heat fluxes, and conductive heat flux could no longer respond to increase in the incoming radiation; hence, all the energy excess went to melting. Melt water that flushed through the draining holes in the sea ice (Figure 2d) drastically lowered the salinity of under ice water (Figure 7e). This fresh surface layer persisted until the end of the study period and is indicative of the loss of meltwater from the surface contributing to sea ice uplift. By 20 June, drainage networks had developed such that they radiated toward holes in the sea ice, characteristic of *melt pond evolution stage 2* (Eicken et al., 2002). The period was marked by a nearly isothermal upper section (50 cm) of sea ice (Figure 7b), rapid desalination of the sea ice (Figure 6a), and the lowest underice salinity recorded over the experiment (Figure 7e).

We note that nighttime refreezing of the surface still occurred, particularly during cloud-free periods, as seen by the drop in surface temperature and the negative atmospheric net energy flux from 19 to 23 June in Figures 4 and 11. For example, a 3- to 4-mm ice layer was observed to have formed on melt ponds on 22 June. The highest recorded air temperature of 5.9 °C occurred on 23 June, when the sky was mostly clear as indicated by low downwelling longwave radiation (L_{in}) values (Figure 9b). This high air temperature likely resulted from advection from land; the maximum air temperature recorded at the nearby Cambridge Bay airport weather station reached 16.6 °C on 23 June (Environment and Climate Change Canada). The cooling (refreezing) of the surface during nighttime was absent after 23 June as seen by the positive net atmospheric energy flux in Figure 11. This positive net atmospheric energy flux was associated with periods of positive net longwave radiation (e.g., 24 June). Although clouds were present, their temperature was significantly above freezing point resulting in the periods of positive net longwave radiation.

4.2. Formation of Superimposed and Interposed Ice

Between transitions II and V, we visibly observed a change in snow grains and texture indicative of melt and melt-freeze metamorphism (Colbeck, 1982). The snow cover had already undergone significant melting on 24 May and 28–29 May associated with the southerly low-pressure systems, with the snowpack reaching isothermal melting temperatures during the latter (Figure 7a). Indeed, ice lenses in the snow along with superimposed ice were observed in a snow pit on 1 June (Figure 5). At this time net radiation (Q^*) fluctuated between positive and negative (Figure 11). Others have suggested that when net radiation is the primary source of energy, the rate of superimposed ice formation is controlled by the surface snow melting rate, the meltwater percolation rate (Cheng et al., 2003; Wadham & Nuttall, 2002; Wakahama et al., 1976), and the heat transfer rate through the snowpack (Boggild, 2007; Granskog et al., 2006). The reversal of the temperature gradient (Transition III) supported the formation of superimposed ice by directing energy from the surface towards the atmosphere (Figures 7a and 7c and 8). Latent heat released during superimposed ice formation was being lost from the relatively warmer snowpack to the colder atmosphere (Figures 4 and 7a and 7c). The accretion of superimposed ice appears to have resulted from the rapid refreezing of snow meltwater on top of the previously formed cold ice layer, similar to processes described by Granskog et al. (2006). The location and thickness of superimposed ice in snow pits (Figure 5) was however variable owing to the characteristic heterogeneity of the snow cover.

From 28 May to 3 June temperature waves propagated down into the ice (Figures 6 and 7a and 7b) even as snow surface temperatures decreased (Figure 4) likely aiding the percolation of meltwater into the upper layer of the sea ice cover and formation of interposed ice. This is evident by the decrease in the salinity and higher temperature of the upper layer of the ice cores (Figure 6). Similar temperatures waves have been described to occur in association with overcast conditions during the winter season producing temperature increments and heat conduction shifts in the sea ice (Persson et al., 2017). Indeed, interior ice temperatures generally continued to rise throughout the study period (Figure 7b) and heat continuously flowed from the warmer snow-ice interface and from the basal layer of sea ice towards the cold middle ice section (Figures 6 and 7a–7c). Temperature profiles showed that between 40- and ~80-cm depth the ice remained colder in comparison to the upper and basal layers. This is corroborated by the continuous thermocouple observations (Figure 7b). Latent heat released on refreezing of the percolated meltwater and associated warming within sea ice pores would have encouraged the water to percolate to a greater depth and/or to spread laterally by aiding melting of the pore channels. It is evident by the changes in salinity, brine volume, and temperature profiles that salt had been *flushed* (Landy et al., 2014) from the upper 10-cm layer of the ice by 5 June and that the depth of interposed ice formation was located at around 20–40 cm below the ice surface (Figure 6). Vancoppenolle et al. (2007) suggested that the desalinization of the upper section of sea ice overlaid by a thick snow cover prompt the formation of an impervious layer. Interposed ice formed in this manner likely played an important role in keeping the ice cover permeability low (Polashenski et al., 2017), thereby contributing to the extensive surface flooding when the snowpack finally melted after 16 June (Figures 1 and 2). The static underwater salinity profile (Figure 7e) and steady underice pressure (Figure 7d) observed between 12 and 16 June and the subtle salinity decrease and comparatively low brine volume change (Figure 6) indicate that meltwater was not drained in significant amounts and that the ice cover indeed was impermeable to meltwater percolation.

Thus, the impermeable surface layer consisted of (i) a layer of superimposed ice at the snow-ice interface (Figure 5) and (ii) interposed ice formed within the near surface portion of the ice (Figure 6) that would effectively close off brine channels within the ice interior (Polashenski et al., 2017). Our field campaign ended before a fully drained sea ice cover was encountered. Based on Landsat and Moderate Resolution Imaging Spectroradiometer (MODIS) imagery, it took until about 9 July for the ice permeability to increase sufficiently such as not to inhibit vertical drainage of surface meltwater (see Figures S4 and S5). Thus, melt pond evolution stage 2 presumably continued until early July.

4.3. The Albedo of Flooded Sea Ice

Aerial imagery suggests a patchy sea ice surface that is shown in Figure 1 made up of bare white ice, flooded lighter blue ice (superimposed ice), and flooded darker blue ice at the beginning of the melt period. The variability in albedo seen on 17 June (albedo over 0.4; Figure 10) reflected the presence of floating slush ice (which was most likely superimposed ice released from the ice interface) and bubble-laden superimposed ice directly beneath meltwater. By 20 June, the bubbles dissipated, and lighter blue and darker blue patches were observed beneath the flooded ice (Figure 1). As meltwater drained, a bubbly fresh white ice—drained superimposed ice—with an albedo ranging from approximately 0.26 to 0.43 emerged above the meltwater surface level (red and green squares to the left in Figure 10). Photographs of these features are shown in Figures 1 and 2. The presence of superimposed ice kept the albedo relatively high.

By 23 June most of the superimposed ice had melted and darker blue ice was generally prevalent beneath the floodwater with typical albedo values of just above 0.2 (Figure 10). Similar observations were reported by Perovich (1996) and Perovich et al. (2002). The decrease in albedo for the fully flooded sea ice surface (Figure 10) had implications for the surface energy budget as seen in Figure 11 (increase in $+F_{net}$), ice warming (melting) rate as seen in Figure 7 (nearly isothermal sea ice), and light transmission through the ice cover (e.g., Katlein et al., 2015).

5. Summary and Conclusions

During this study of the landfast sea ice in Dease Strait in the CAA, we observed the transition of the sea ice from a cold snow-covered premelt state to a nearly 100% meltwater flooded state (Movie S1) and were able to relate these changes to terms in the surface energy budget. Scientific observations and surface-based studies over near fully flooded sea ice (>70–80% pond fraction) are unique (Polashenski et al., 2012). This

flooding makes travel and use of the landfast ice platform difficult and often restricted to nighttime (Laidler et al., 2008). By combining the time series of meteorological and radiative data collected by the MET tower with visual and physical observations of the study area, it was possible to identify five distinct seasonal transitions during this progression: (I) winter to spring transition, (II) snowfall event, (III) melt hiatus, (IV) melt onset, and (V) melt pond formation. These key periods in the melt process were connected to the passage of transient low-pressure systems through their effect on air temperature and components of the energy budget. Our results suggest that the impact of transient weather events on the progression of melt depends on the magnitude and advection of air associated with the direction of movement of the low-pressure system, the intensity of the event, and its associated weather conditions. As opposed to the uniform progression of sea ice melt presented in previous studies (e.g., Else et al., 2014), the 2014 melt season in Dease Strait was interrupted by a particularly prominent sequence of events that started with the passage of a low-pressure system that brought heavy snowfall and was succeeded by brief cooling periods and ultimately return to colder weather (melt hiatus). Without this sequence of events, that prompted the widespread formation of an impermeable layer and provided a larger meltwater reservoir, melt pond formation would have likely commenced in the first week of June and presumably led to a less extensive melt pond areal coverage in the study area.

Our results indicate that the extensive flooding observed in Dease Strait was made possible because of the flatness of the landfast ice surface (Landy et al., 2015) and the described sequence of weather events that led to the formation of superimposed and interposed ice that acted to reduce over-all sea ice permeability. The 2-week delay in the melt onset may have further accentuated the rate of melt once initiated. Visual observations and spectral albedo measurements confirmed that the albedo of the snow-free ice surface was highly sensitive to the presence of superimposed ice. Indeed, patchiness in superimposed ice gave rise to spatial variability in surface albedo of flooded areas (Figures 1 and 10). This variability persisted until the features eroded, after which uniformly low albedo was observed across the flooded portion of the ice cover. The late-season time series of underice pressure and seawater salinity in combination with the ice core measurements of bulk salinity provide evidence that the sea ice was impermeable and that vertical percolation through the ice was not taking place during the study time. Our results suggest that continuous heat storage in the meltwater cover areas lead to superimposed ice breaking off from pond bases before the sea ice became permeable; thus, interposed ice must have been a key factor in reducing the permeability of sea ice. Future challenges remain to quantitatively measure the presence of superimposed ice and interposed ice layers and to better understand their effect on sea ice permeability, while sea ice temperatures are near the melting point.

With Arctic-wide trends toward earlier melt onset (Stroeve et al., 2014) and declining sea ice extent and thickness (Maslanik et al., 2007; Perovich & Richter-Menge, 2009), the Arctic sea ice environment is becoming more vulnerable to the effects of episodic forcing associated with transient weather events (Simmonds & Keay, 2009; Tilinina et al., 2014). Based on the results of this study, we expect corresponding effects on the timing and duration of Arctic sea ice melt with broader ecosystem and societal implications, including access to modes of safe transportation and travel on the sea ice in proximity to northern communities. Further temporal and spatial studies are needed to better understand and predict (1) the processes producing episodic atmospheric forcing, (2) the effects of episodic forcing during the progression of melt, (3) the formation of superimposed and interposed ice as a result of varying energy balance components, (4) the role of superimposed and interposed ice in the formation and maintenance of melt ponds, and (5) the role of isostatic adjustment of sea ice during the evolution of melt ponds. Given the complex role that atmospheric processes (e.g., episodic forcing, CRF, and precipitation events) can have on an ongoing changing sea ice, developing robust coupled models that include these processes and physical processes such as ice rebound and snow melting/refreezing may provide an efficient simulation of sea ice seasonal evolution allowing us to identify major parameters driving sudden changes.

Acknowledgments
We gratefully acknowledge the logistical support of the Canadian High Arctic Research Station (CHARS), the Hunter's and Trapper's Organization (HTO), and airport staff in Cambridge Bay. We would like to thank research teams involved in the ICE-CAMPS 2014 project and particularly C. J. Mundy, A. Delaforge, and S. P. Luque. We are also grateful for instrument support by D. Barber. This study was funded by the NCE ArcticNet and Natural Sciences and Engineering Research (NSERC) grants to J. K. E. and T. N.P. This work is a contribution to the Canada Excellence Research Chair (CERC) to S. Rysgaard, and to the Arctic Science Partnership (ASP) asp-net.org. Data are available for academic purposes through the CanWIN Data HUB portal (http://lwbin-datahub.ad.umanitoba.ca/dataset/ic-2014-diaz-meltwater).

References

Boggild, C. E. (2007). Simulation and parameterization of superimposed ice formation. *Hydrological Processes*, *21*(12), 1561–1566. https://doi.org/10.1002/hyp.6718

Cheng, B., Launianen, J., & Vihma, T. (2003). Modelling of superimposed ice formation and sub-surface melting in the Baltic Sea. *Geophysica*, *39*(1–2), 31–50.

Colbeck, S. C. (1982). An overview of seasonal snow metamorphism. *Reviews of Geophysics and Space Physics*, *20*(1), 45–61. https://doi.org/10.1029/RG020i001p00045
Cox, G. F. N., & Weeks, W. F. (1983). Equations for determining gas and brine volumes in sea ice samples. *Journal of Glaciology*, *29*(102), 306–316. https://doi.org/10.1017/S0022143000008364
Ehn, J. K., Granskog, M. A., Papakyriakou, T., Galley, R., & Barber, D. G. (2006). Surface albedo observations of Hudson Bay (Canada) landfast sea ice during the spring melt. *Annals of Glaciology*, *44*, 23–29. https://doi.org/10.3189/172756406781811376
Eicken, H., Krouse, H. R., Kadko, D., & Perovich, D. K. (2002). Tracer studies of pathways and rates of meltwater transport through Arctic summer sea ice. *Journal of Geophysical Research*, *107*(C10), 8046. https://doi.org/10.1029/2000JC000583
Else, B. G. T., Papakyriakou, T. N., Raddatz, R., Galley, R. J., Mundy, C. J., Barber, D. G., et al. (2014). Surface energy budget of landfast sea ice during the transitions from winter to snowmelt and meltpond onset: The importance of net longwave radiation and cyclone forcing. *Journal of Geophysical Research: Oceans*, *119*, 3679–3693. https://doi.org/10.1002/2013JC009772
Flato, G. M., & Brown, R. D. (1996). Variability and climate sensitivity of landfast Arctic sea ice. *Journal of Geophysical Research*, *101*(C10), 767–777.
Galley, R. J., Else, B. G. T., Howell, S. E. L., Lukovich, J. V., & Barber, D. G. (2012). Landfast sea ice conditions in the Canadian Arctic: 1983–2009. *Arctic*, *65*(2), 133–144.
Granskog, M. A., Vihma, T., Pirazzini, R., & Cheng, B. (2006). Superimposed ice formation and surface energy fluxes on sea ice during the spring melt-freeze period in the Baltic Sea. *Journal of Glaciology*, *52*(176), 119–127. https://doi.org/10.3189/172756506781828971
Haas, C., Bareiss, J., & Nicolaus, M. (2002).z The surface energy balance and its importance for superimposed ice formation (SEBISUP). (EC-LSF Report NP-9/2001).
Horner, R., Ackley, S. F., Dieckman, G. S., Gulliksen, B., Hoshiai, T., Legendre, L., et al. (1992). Ecology of sea ice biota: 1. Habitat, terminology, and methodology. *Polar Biology*, *12*, 417–427.
Iacozza, J., & Barber, D. G. (2001). Ablation patterns of snow cover over smooth first-year sea ice in the Canadian Arctic. *Hydrological Processes*, *15*(18), 3559–3569. https://doi.org/10.1002/hyp.1037
Intrieri, J. M., Fairall, C. W., Shupe, M. D., Persson, P. O. G., Andreas, E. L., Guest, P. S., & Moritz, R. E. (2002). An annual cycle of Arctic surface cloud forcing at SHEBA. *Journal of Geophysical Research*, *107*(C10), 8039. https://doi.org/10.1029/2000JC000439
Katlein, C., Arndt, S., Nicolaus, M., Perovich, D. K., Jakuba, M. V., Suman, S., et al. (2015). Influence of ice thickness and surface properties on light transmission through Arctic sea ice. *Journal of Geophysical Research: Oceans*, *120*, 5932–5944. https://doi.org/10.1002/2015JC010914
Kawamura, T., Jeffries, M. O., Tison, J.-L., & Krouse, H. R. (2004). Superimposed-ice formation in summer Ross Sea pack-ice floes. *Annals of Glaciology*, *39*, 563–568. https://doi.org/10.3189/172756404781814168
Koerner, R. M. (1970). Some observations on superimposition of ice on the Devon Island ice cap, N.W.T., Canada. *Geografiska Annaler. Series A, Physical Geography*, *52*(1), 57–67.
Laidler, G. J., Dialla, A., & Joamie, E. (2008). Human geographies of sea ice: Freeze/thaw processes around Pangnirtung, Nunavut, Canada. *Polar Record*, *44*(04), 335–361. https://doi.org/10.1017/S003224740800750X
Landy, J. C., Ehn, J. K., & Barber, D. G. (2015). Albedo feedback enhanced by smoother Arctic sea ice. *Geophysical Research Letters*, *42*, 10,714–10,720. https://doi.org/10.1002/2015GL066712
Landy, J. C., Ehn, J. K., Shields, M., & Barber, D. G. (2014). Surface and meltpond evolution on landfast first-year sea ice in the Canadian Arctic Archipelago. *Journal of Geophysical Research: Oceans*, *119*, 3054–3075. https://doi.org/10.1002/2013JC009617
Leppäranta, M., & Manninen, T. (1988). *The brine and gas content of sea ice with attention to low salinities and high temperatures*. Helsinki, FI: Finish Institute of Marine Research.
Leu, E., Mundy, C. J., Assmy, P., Campbell, K., Gabrielsen, T. M., Gosselin, M., et al. (2015). Arctic spring awakening-steering principles behind phenology of vernal ice algal blooms. *Progress in Oceanography*, *139*, 151–170. https://doi.org/10.1016/j.pocean.2015.07.012
Leuning, R., van Gorsel, E., Massman, W. J., & Isaac, P. R. (2012). Reflections on the surface energy imbalance problem. *Agricultural and Forest Meteorology*, *156*, 65–74. https://doi.org/10.1016/j.agrformet.2011.12.002
Male, D. H., & Granger, R. J. (1981). Snow surface energy exchange. *Water Resources Research*, *17*(3), 609–627. https://doi.org/10.1029/WR017i003p00609
Maslanik, J. A., Fowler, C., Stroeve, J., Drobot, S., Zwally, J., Yi, D., & Emery, W. (2007). A younger, thinner Arctic ice cover: Increased potential for rapid extensive sea-ice loss. *Geophysical Research Letters*, *34*, L24501. https://doi.org/10.1002/2013GL058951
Melling, H. (2002). Sea ice of the northern Canadian Arctic Archipelago. *Journal of Geophysical Research*, *107*(C11), 3181. https://doi.org/10.1029/2001JC001102
Mortin, J., Svensson, G., Graversen, R. G., Kapsch, M.-L., Stroeve, J. C., & Boisvert, L. N. (2016). Melt onset over Arctic sea ice controlled by atmospheric moisture transport. *Geophysical Research Letters*, *34*, 6636–6642. https://doi.org/10.1029/2007GL032043
Nicolaus, M., Haas, C., & Bareiss, J. (2003). Observations of superimposed ice at melt-onset on fast ice on Kongsfjorden, Svalbard. *Physics and Chemistry of the Earth*, *28*(28-32), 1241–1248. https://doi.org/10.1016/j.pce.2003.08.048
Oke, T. R. (1987). *Boundary layer climates* (2nd ed.) Routledge: Taylor & Francis Group.
Papakyriakou, T. (1999). An examination of relationship among the energy balance, surface properties and climate over snow covered sea ice during the spring season, (PhD thesis). Waterloo, ON: University of Waterloo.
Perovich, D. K. (1996). *The optical properties of sea ice. (Monograph 96–1)*. Arlington, VA: US Army Corps of Engineers Cold Regions Research & Engineering Laboratory.
Perovich, D. K., Grenfell, T. C., Light, B., & Hobbs, P. V. (2002). Seasonal evolution of the albedo of multiyear Arctic sea ice. *Journal of Geophysical Research*, *107*(C10), 8044. https://doi.org/10.1029/2000JC000438
Perovich, D. K., Grenfell, T. C., Richter-Menge, J. A., Light, B., Tucker, W. B. III, & Eicken, H. (2003). Thin and thinner: Sea ice mass balance measurements during SHEBA. *Journal of Geophysical Research*, *108*(C3), 8050. https://doi.org/10.1029/2001JC001079
Perovich, D. K., & Polashenski, C. (2012). Albedo evolution of seasonal Arctic sea ice. *Geophysical Research Letters*, *39*, L08501. https://doi.org/10.1029/2012GL051432
Perovich, D. K., Polashenski, C., Arntsen, A., & Stwertka, C. (2017). Anatomy of a late spring snowfall on sea ice. *Geophysical Research Letters*, *44*, 2802–2809. https://doi.org/10.1002/2016GL071470
Perovich, D. K., & Richter-Menge, J. A. (2009). Loss of sea ice in the Arctic. *Annual Review of Marine Science*, *1*(1), 417–441. https://doi.org/10.1146/annurev.marine.010908.163805
Persson, P. O. G. (2012). Onset and end of the summer melt season over sea ice: Thermal structure and surface energy perspective from SHEBA. *Climate Dynamics*, *39*(6), 1349–1371. https://doi.org/10.1007/s00382-011-1196-9
Persson, P. O. G., Shupe, M. D., Perovich, D., & Solomon, A. (2017). Linking atmospheric synoptic transport, cloud phase, surface energy fluxes, and sea ice growth: Observations of midwinter SHEBA conditions. *Climate Dynamics*, *49*(4), 1341–1364. https://doi.org/10.1007/s00382-016-3383-1

Polashenski, C., Golden, K. M., Perovich, D. K., Skyllingstad, E., Arnsten, A., Stwertka, C., & Wright, N. (2017). Percolation blockage: A process that enables melt pond formation on first year Arctic sea ice. *Journal of Geophysical Research: Ocean*, *122*, 413–440. https://doi.org/10.1002/2016JC011994

Polashenski, C., Perovich, D., & Courville, Z. (2012). The mechanisms of sea ice formation and evolution. *Journal of Geophysical Research*, *117*, C01001. https://doi.org/10.1029/2011JC007231

Pringle, D. J., Eicken, H., Trodahl, H. J., & Backstrom, L. G. E. (2007). Thermal conductivity of landfast Antarctic and Arctic sea ice. *Journal of Geophysical Research*, *112*, C04017. https://doi.org/10.1029/2006JC003641

Simmonds, I., & Keay, K. (2009). Extraordinary September Arctic sea ice reductions and their relationships with storm behaviour over 1979-2008. *Geophysical Research Letters*, *36*, L19715. https://doi.org/10.1029/2009GL039810

Stroeve, J. C., Markus, T., Boisvert, L., Miller, J., & Barret, A. (2014). Changes in Arctic melt season and implications for sea ice loss. *Geophysical Research Letters*, *41*, 1216–1225. https://doi.org/10.1002/2013GL058951

Sturm, M., Holmgren, J., König, M., & Morris, K. (1997). The thermal conductivity of seasonal snow. *Journal of Glaciology*, *43*(143), 26–41. https://doi.org/10.1017/S0022143000002781

Tilinina, N., Gulev, S. K., & Bromwich, D. H. (2014). New view of Arctic cyclone activity from the Arctic system reanalysis. *Geophysical Research Letters*, *41*, 1766–1772. https://doi.org/10.1002/2013GL058924

Vancoppenolle, M., Bitz, C. M., & Fichefet, T. (2007). Summer landfast sea ice desalinisation at Point Barrow, Alaska: Modeling and observations. *Journal of Geophysical Research*, *112*, C04022. https://doi.org/10.1029/2006JC003493

Wadham, J. L., & Nuttall, A.-M. (2002). Multiphase formation of superimposed ice during a mass-balance year at a maritime high-Arctic glacier. *Journal of Glaciology*, *48*(163), 545–551. https://doi.org/10.3189/172756502781831025

Wakahama, G., Kuroiwa, D., & Hasemi, T. (1976). Field observations and experimental and theoretical studies on the superimposed ice of McCall Glacier, Alaska. *Journal of Glaciology*, *16*(74), 135–149. https://doi.org/10.1017/S0022143000031488